Composites: Part A 149 (2021) 106564

Contents lists available at ScienceDirect

Composites Part A

journal homepage: www.elsevier.com/locate/compositesa

Influence of curing processes on the development of fiber bridging during delamination in composite laminates

Ping Hu[1], Ditho Pulungan[1], Ran Tao[1], Gilles Lubineau[1,*]

King Abdullah University of Science and Technology (KAUST), Physical Science and Engineering Division, COHMAS Laboratory, Thuwal 23955-6900, Saudi Arabia

ARTICLE INFO

Keywords:
Fiber bridging
Degree of curing
Delamination
Double cantilever beam

ABSTRACT

Fiber bridging can significantly influence the interlaminar toughness of laminated composites. However, very little is known about to what extent it depends on the processing conditions. In this paper, we performed a back-bonded double cantilever beam (BB-DCB) test to study the curing process influence on the development of fiber bridging for composite laminates with various thicknesses. The BB-DCB sample included a middle core plate and two backing adherends bonded to each side of the core plate. The total thickness of the BB-DCB samples was kept the same to guarantee the same structural effect due to beam curvature. Thus, only the core plate thickness effect was varied and studied. The experimental results showed that the core plate thickness significantly influences fiber bridging, as the samples with thicker core plates triggered more fiber bridging. Differential scanning calorimetry (DSC) was used to evaluate the degree of cure (DoC) for the different thicknesses, and a correlation was shown between the DoC and the fiber bridging extent. An embedded cell approach was also adopted to show that more fiber bridging was triggered with a larger variance of the fiber/matrix interface toughness and strength, which might have resulted from the change in the DoC with the plate thickness.

1. Introduction

Delamination damage in laminated composites has been widely studied due to the weakness of these materials under out-of-plane loading. The properties at the onset and propagation of delamination are ascribed to the contributions of both local material properties and non-local structural effects, *i.e.,* fiber bridging [1–4]. During the growth of a delamination front, fibers inside the laminates are pulled out, and fracture surfaces are bridged. This can be seen as a positive phenomenon, as it has the potential of significantly toughening the interface [5–9]. However, it should also be acknowledged that such phenomena complexify the modeling that should account for the development of bridging and its effects on interlaminar cohesive tractions [10–12].

The development of fiber bridging is usually easy to detect, as it results in a rising resistance curve (R-curve). The initial toughness depends on the material property of the fiber/matrix interface, while the way the R-curve increases mainly depends on the fiber bridging extent [1]. Thus, the R-curve is mainly the result of structural effects rather than material property. Farmand et al. [13] implemented a series of DCB tests using specimens with different thicknesses. They found that more bridging appeared during the delamination propagation for thicker specimen, leading to a higher toughness at the plateau level of the R-curve. The sample thickness influences the DCB beam curvature, which changes the bridging traction decay rate in the fiber bridging zone. Frossard et al. [14] conducted DCB tests on specimens with the same total thickness but with plies of different thicknesses and microstructures. Their results indicated that the microstructure of a laminate influence the formation and development of fiber bridging. Laminates made with thin-ply composites have a relatively uniform microstructure, leading to a flat delamination surface with much less fiber bridging compared with thick-ply composites. More generally, the origin of fiber bridging comes from the spatial variability of the interlaminar properties over a delamination interface, including defects or the yield zone in a crack tip [1]. Such variabilities can for instance, result from nesting where the fibers of adjacent plies migrate, causing a curved mid-plane after curing [15]. This happens during manufacturing processes, and it is well known as one source of triggering fiber bridging. Tao et al. [16] implemented a simulation work to trigger ligaments by introducing heterogeneity in the framework of secondary bonded joints, and they found that a certain level of spatially-varying interface properties can help in forming adhesive ligaments, leading

* Corresponding author.
E-mail address: gilles.lubineau@kaust.edu.sa (G. Lubineau).

[1] All authors contributed to writing and editing the manuscript.

https://doi.org/10.1016/j.compositesa.2021.106564
Received 7 March 2021; Received in revised form 11 July 2021; Accepted 13 July 2021
Available online 19 July 2021
1359-835X/

to bridging zones for crack-arrest. Meanwhile, the numerical research of Li et al. [17,18] showed that the variability in the statistically uniform properties of an interface has a significant influence on the adhesive ligaments in secondary bonded joints. Herráez et al. [19] enhanced the fracture toughness of delamination by introducing small interlaminar defects to promote fiber bridging. More recently, Liu et al. [20] proposed a theoretical model to determine the occurrence of fiber bridging based on a weak fiber/matrix interface mechanism. They compared the actual ultimate transverse tensile strength with the predicted transverse tensile strength calculated using a perfectly bonded fiber/matrix interface assumption. The experiments proved that fiber bridging occurs when the predicted transverse tensile strength is obviously higher than the actual one. Overall, these works indicated the importance of heterogeneity in promoting fiber bridging during delamination propagation.

Due to the low through-thickness thermal conductivity [21,22], a source of variability in the distribution of interfacial properties is the difference in curing when the thickness of a specimen is changed. The gradient in the curing state is a topic that has been extensively investigated. Li et al. [23] found that specimen thickness is an important factor that influences temperature distribution through the thickness direction using microwave curing technologies. For a thick laminate of 22.5 mm, there was almost a temperature difference of 10°C between the top and bottom surfaces. Meanwhile, this might also result in strong variations in the degree of cure (DoC) of CFRP plates. W. Stark et al. [24] studied the relationship between DoC and the curing time at 180°C, and their results showed that curing reactions happen in the first 60 min mainly with a DoC of 0.85 at 2 h, while 5 h are needed for a full cure. An incomplete cure might result in less uniform interface properties. Therefore, a legitimate question arises about the effects of the processing condition and DoC on the interlaminar properties distribution and the resulting bridging effect. Chris et al. [25] studied the influence of cure path on the Mode I fracture behavior in thermoplastic particle interleaf toughened composites. A reduction by 11%–22% of the Mode I toughness was observed by incorporating a dwell stage before reaching the final cure temperature. Also, recent research by Cheng et al. [26] studied the cure path dependency of the Mode II fracture of interlayer toughened composites. The thermoplastic particles and interlayer thickness were varied with different cure cycles, which influenced the Mode II fracture behavior. The curing rate of epoxy fiberglass composites could also change its microstructure. Patel et al. [27] found that samples with sufficient pre-cure cycle, which allows gel completely before post-curing, had an homogeneous microstructure. In contrast, samples with faster curing featured a non-homogeneous microstructure, which significantly influenced the fatigue life of composite structures due to the stress concentration resulting from the softer phase inclusions. Hoffman et al. [28] also pointed that higher oven temperature led to a shorter curing time and higher residual strain in a single fiber/polymer composite curing system. However, to the authors' knowledge, the curing process's influence on the development of fiber bridging was not fully discussed in the literature.

In this work, we designed an experimental campaign to study the curing process's effect on the development of fiber bridging. To exclude the structural effect influence on bridging traction, we operated a series of the back-bonded double cantilever beam (BB-DCB) tests so that all specimens always shared the same total thickness. The BB-DCB sample included a middle core plate and two backing adherends, which were cured in separate batches and then bonded together to the same total thickness. Since the delamination crack propagated in the middle interface of the core plate, the only factor that influenced the development of fiber bridging was the curing process of core plates with different thicknesses. Meanwhile, the curing degree of these plates was evaluated and correlated with Mode I fracture toughness. We also provided simulation work to illustrate the plausible reasons for the thickness-dependent fiber bridging phenomena found in the experiments based on the change in the fracture properties variability over the interface.

Section 2 describes the experimental strategy, sample preparation, and results of the BB-DCB tests. Section 3 shows our interpretation of the experimental results and uses an embedded cell model [29] to analyze the influence of fiber/matrix strength and toughness variability on the R-curve performance. Section 4 concludes this work and shows our future research directions.

2. Experiments

2.1. Materials and specimens

Hexply T700/M21 with a nominal cured thickness of 0.25 mm was used as the carbon/epoxy prepreg for fabricating the BB-DCB samples. Panels of 300 mm × 300 mm square prepregs with a fiber volume fraction of 57% were manually stacked with a specific sequence. One bar vacuum was applied to extract air after manually stacking the prepregs. The lay-ups were then cured using a hydraulic hot-press machine (Pinette Emidecau Industries 15T) for 2 h at 180°C at a heating speed of 2°C/min and were then cooled down to room temperature at a cooling speed of −3°C/min. The curing process was under a gauge pressure of seven bar and one bar vacuum environment.

The cured plates were cut using a Protomax water-jet cutting machine to manufacture the backing adherends and core samples. The backing adherends were bonded to the core sample using a rapid two-component epoxy glue Araldite 420. Uniform pressure was applied over the BB-DCB sample using clamps at a constant temperature (60°C) during the back bonding process. Four different stacking sequences were chosen for the BB-DCB tests to study the curing effect: $[0_8]_s$, $[0_2 \parallel 0_6]_s$, $[0_4 \parallel 0_4]_s$ and $[0_6 \parallel 0_2]_s$, where the symbol '||' denotes the back bonding position. Each configuration has six samples tested. Fig. 1(a)–(d) show the schematic and side view of the unidirectional BB-DCB samples after manufacturing. In the end, the BB-DCB samples were 250 mm long and 20 mm wide with a 50-mm long pre-crack, where an aluminum foil was inserted the prepregs were manually stacked. The total thickness of $[0_8]_s$ was 4 mm, while the BB-DCB samples were 4.2 mm thick due to the extra Araldite epoxy layer. The difference in the structural effect on the bridging development for the 4-mm and 4.2-mm thick beam samples could be neglected. The exact geometrical characteristics of each sample were recorded before testing for data reduction. Then, aluminum blocks were bonded to the BB-DCB sample for load transfer. The DCB tests were operated in an Instron 5882 test frame (500 N load cell) at a speed of 2 mm/min according to the ASTM standard D5528 [30]. On each sample, one edge was marked with white lines at every millimeter. A DSLR camera recorded the delamination crack length and fiber bridging extent. The compliance calibration (CC) [30] method was used for data reduction to calculate the interlaminar Mode I toughness. As a note, data reduction methods given in the standard are usually applied in cases with a smooth delamination surface. When fiber bridging exists, it is not accurate since the cracked interface is still linked by the bridging fibers. Frossard et al. [31], and Pappas et al. [32] used double compliance calibration (DCC) and modified power law (MPL) method to consider the effect of fiber bridging on compliance fitting, which gives a proper toughness evaluation. While the difference between different data reduction methods is not very big for unidirectional DCB tests. In this work, for the sake of comparison between different curing conditions, a small error is acceptable when using the CC method.

To exclude the back bonding effect on the fiber bridging development in the BB-DCB sample, an additional test was designed, as illustrated in Fig. 2, for the specific case of the $[0_6 \parallel 0_2]_s$ stacking sequence. Instead of curing the core plate and backing adherend plates in separate batches, we cured them altogether in one batch while separated with aluminum foils. After the curing process, the core plate and backing adherend plates could be easily separated. Then, we used

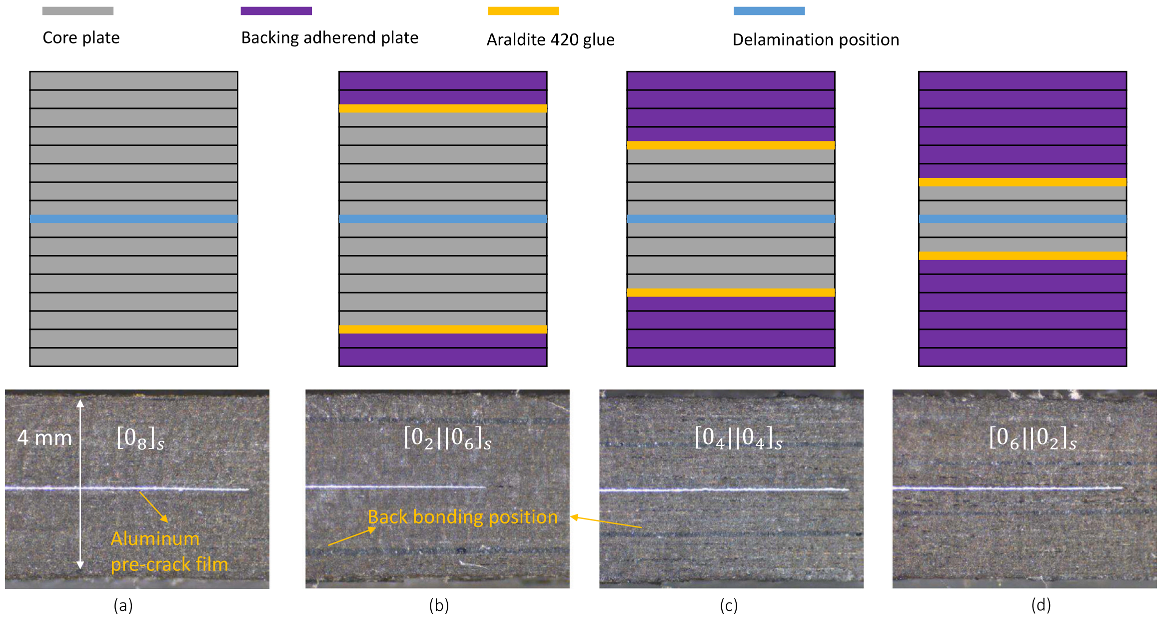

Fig. 1. Schematic and side view of the BB-DCB samples after manufacturing.

Table 1
Samples of the separately-cured and co-cured plates, where '|||' denotes aluminum foil.

Separately-Cured plates	Back bonded samples
core $[0_8]_s$	without back bonding
backing adherend $[0_2]$, core $[0_6]_s$	$[0_2 \parallel 0_6]_s$
backing adherend $[0_4]$, core $[0_4]_s$	$[0_4 \parallel 0_4]_s$
backing adherend $[0_6]$, core $[0_2]_s$	$[0_6 \parallel 0_2]_s$
Co-Cured plates	
$[0_6|||0_4|||0_6]$	$[0_6 \parallel 0_2]_s$ (co-cured)

the same back bonding process to bond the backing adherends and core plate. This kind of sample is referred as co-cured $[0_6 \parallel 0_2]_s$, which is distinguished with the separately-cured $[0_6 \parallel 0_2]_s$. Table 1 shows the samples of separately-cured and co-cured plates. Therefore, the only difference between the separately-cured $[0_6 \parallel 0_2]_s$ BB-DCB sample and co-cured $[0_6 \parallel 0_2]_s$ BB-DCB sample was the plate thickness during the hot-press curing process. The toughness and image view of the bridging result of the separately-cured $[0_6 \parallel 0_2]_s$ and co-cured $[0_6 \parallel 0_2]_s$ BB-DCB samples were then compared.

Curing degree evaluation

To check the variation in curing between the samples with various thicknesses, a Netzsch instrument DSC 204 HP was used to perform differential scanning calorimetry (DSC). A DSC test was performed with a heating rate of 5°C/min from 100°C to 300°C. Four sets of samples were prepared for the DSC tests, including the uncured prepreg, 1-mm thick plate $[0_2]_s$, 4-mm thick plate $[0_8]_s$ cured for 2 h at 180 °C, and 4-mm thick plate $[0_8]_s$ cured for 4 h at 180 °C. The sample mass was in the range of 6 to 7 mg, and it was cut from different positions of the CFRP plate through its whole thickness. The uncured prepreg was used to obtain the total curing enthalpy H_T. The DoC was defined as $\alpha = 1 - \frac{H_R}{H_T}$, where H_R is the residual enthalpy of the partially cured samples.

Curing time is also a factor that is evaluated to further prove the relationship between the fiber bridging extent and polymerization quality. The 4-mm thick plate $[0_8]_s$ cured for 4 h was also operated in the DCB tests and compared with DCB results of the 4-mm thick plate $[0_8]_s$ cured for 2 h. Table 2 shows the samples for curing degree evaluation.

Table 2
Samples for the curing degree evaluation.

Curing 2 h at 180 °C	Usage
1 mm thick $[0_2]_s$	DSC
4 mm thick $[0_8]_s$	DSC
Curing 4 h at 180 °C	
4 mm thick $[0_8]_s$	DSC and DCB

2.2. Separately-cured BB-DCB results

Fig. 3(a)–(d) show the side view of the four separately-cured BB-DCB samples during DCB loading: $[0_8]_s$, $[0_2 \parallel 0_6]_s$, $[0_4 \parallel 0_4]_s$, and $[0_6 \parallel 0_2]_s$. We compared the bridging extent of these four sequences when the delamination crack reached ∼120 mm. This also corresponded to the steady-state configuration when the fiber bridging became stable. As shown in Fig. 3(a)–(d), the fiber bridging extent at the same delamination crack length decreased with the thinner core plate.

Fig. 4(a) shows the raw data of the original reaction force-opening curve obtained from the 500 N load frame of Instron 5882. The reaction force was obviously higher for the thicker core plate sample that exhibited extensive fiber bridging. Fig. 4(b) shows the interlaminar toughness calculated using the CC method. The plateau in the R-curve indicates the toughness when a stable fiber bridging zone was developed. With extensive fiber bridging triggered, the toughness of $[0_8]_s$ could reach 0.7–0.8 N/mm. Meanwhile, for the thinnest core plate $[0_6 \parallel 0_2]_s$, nearly no fiber bridging was observed, as shown in Fig. 3(d). Therefore, the toughness was as low as ∼0.25–0.3 N/mm. This value corresponds to the classical one expected in the T700/M21 system when classical interfacial failure was observed [33]. The relationship between extensive fiber bridging and increasing toughness was also observed in Moura's et al. research [3]. They studied the effect of bridging on the R-curve by cutting bridging fibers during the DCB loading, which showed that the bridging phenomena were responsible for 60% dissipated energy during delamination propagation in their results.

To get a clearer trend of the toughness with respect to the thickness of the core plate, we defined the propagation toughness as the average toughness of the incremental delamination crack length of 60 mm until the end of the tests, which was seen as a stable delamination

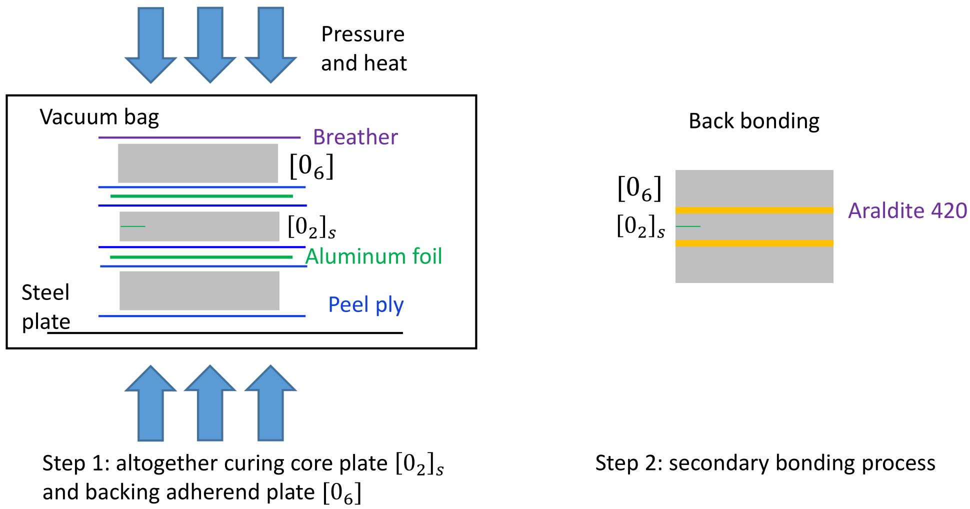

Fig. 2. Schematic of the core plate and backing adherend plates cured altogether in one batch.

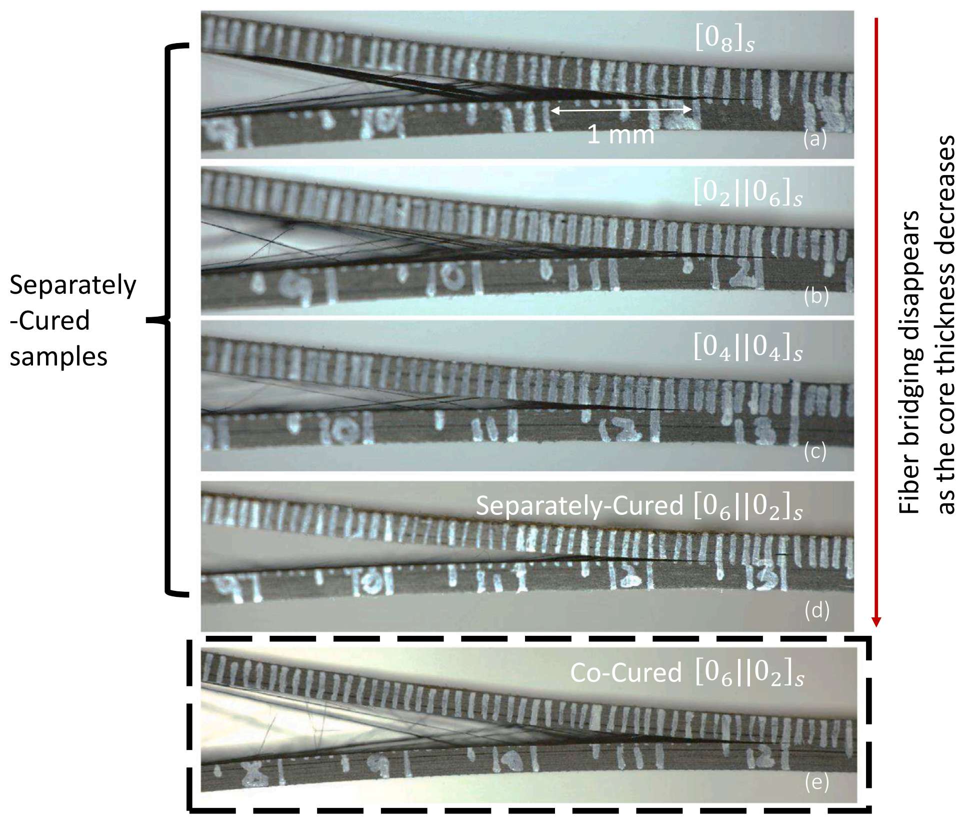

Fig. 3. Fiber bridging extents of the BB-DCB samples with four different core plate thicknesses when the delamination crack increment reached ~120 mm.

propagation zone. Fig. 5 shows the propagation toughness G_{IC}^{prop} of all the samples. There was some expected dispersion in the data. For example, sample 7 had a quite low toughness (0.35 N/mm) compared with the other samples in the $[0_2 \parallel 0_6]_s$ data set. This was due to the randomness of the fiber bridging mechanism. However, the evolution of the propagation toughness with respect to the core plate thickness was clear. In Fig. 4, the fluctuation of the R-curve of the samples with extensive fiber bridging was quite big. This was due to the formation of new fiber bridging and vanished of old fiber bridging, which could be a source of the variance in Fig. 5. Table 3 shows the mean and standard deviation of the propagation toughness of different sets of samples. With the decrease of core plate thickness, the average G_{IC}^{prop} reduced from 0.679 N/m (separately-cured $[0_8]$) to 0.35 N/m (separately-cured $[0_6 \parallel 0_2]$). The standard deviation of G_{IC}^{prop} of the separately-cured sample also decreased with the decrease of core plate thickness, which was due to the stochastic nature of fiber bridging.

2.3. Co-cured BB-DCB results

In the previous section, we illustrated how the extent of fiber bridging largely varied with the core plate thickness when core and backing adherends were cured separately. We observed a reduced toughening effect in the case of thin cores, and in particular for the $[0_6 \parallel 0_2]_s$ sample that has the thinnest core.

In this section, we compared the results of separately-cured $[0_6 \parallel 0_2]_s$ BB-DCB samples (previous section) with those of the co-cured $[0_6 \parallel$

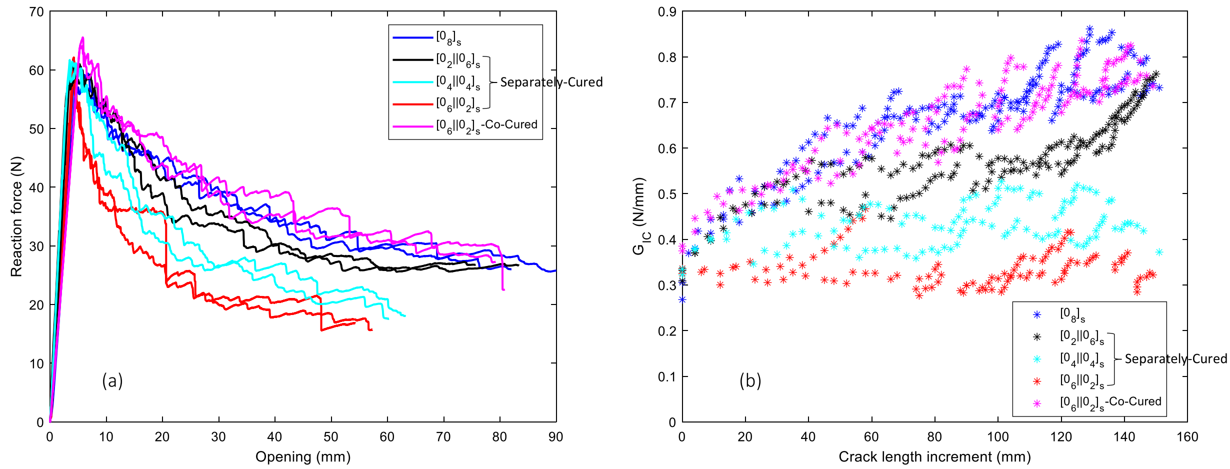

Fig. 4. Interlaminar response of the four sets of BB-DCB tests: (a) reaction force-opening curve, (b) R-curve. (For interpretation of the references to color in this figure legend, the reader is referred to the web version of this article.)

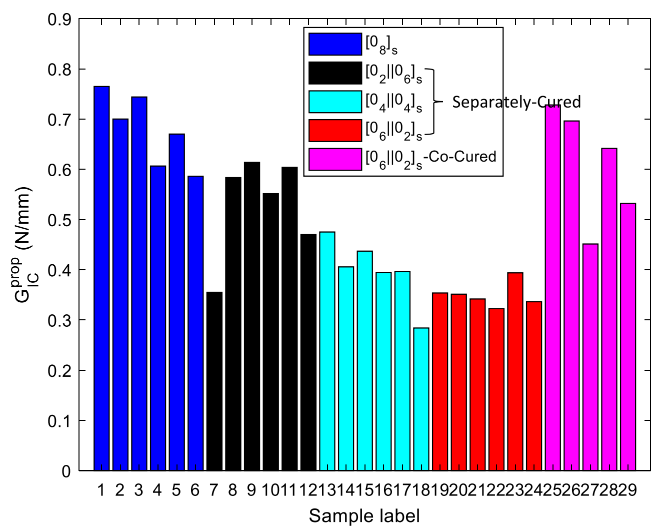

Fig. 5. Propagation toughness G_{IC}^{prop} of the four different sets of BB-DCB samples.

Table 3
Mean and standard deviation value of the propagation toughness G_{IC}^{prop}.

Separately-Cured samples	Average G_{IC}^{prop} (N/mm)	Standard deviation (N/mm)
$[0_8]_s$	0.679	0.072
$[0_2 \parallel 0_6]_s$	0.530	0.100
$[0_4 \parallel 0_4]_s$	0.399	0.064
$[0_6 \parallel 0_2]_s$	0.350	0.024
Co-Cured samples		
$[0_6 \parallel 0_2]_s$	0.610	0.116
Prolong curing time (4 h)		
$[0_8]_s$	0.415	0.023

$0_2]_s$ BB-DCB samples, whose thickness during curing was much larger. The image of the co-cured $[0_6 \parallel 0_2]_s$ BB-DCB sample (Fig. 3(e)) shows more fiber bridging compared with the separately-cured $[0_6 \parallel 0_2]_s$ BB-DCB sample (Fig. 3(d)). The fiber bridging extent between the $[0_8]_s$ (Fig. 3(a)) configuration and co-cured $[0_6 \parallel 0_2]_s$ sample (Fig. 3(e)) was quite similar. The force–displacement curve and R-curve of the $[0_8]_s$ sample and co-cured sample $[0_6 \parallel 0_2]_s$ were at the same level, as shown by the blue and magenta curves in Fig. 4(a) and (b). These results prove that the sample thickness during the curing process was the reason for different fiber bridging phenomena and not the back bonding effect.

Fig. 5 shows the propagation toughness G_{IC}^{prop} of all the tested samples. The toughness values for the stable propagation stage of the $[0_8]_s$ and co-cured $[0_6 \parallel 0_2]_s$ samples were very close, both in the range of 0.6–0.7 N/mm. The average and standard deviation of the propagation toughness of the co-cured $[0_6 \parallel 0_2]$ samples are shown in Table 3. The big deviation value is due to the large scale of fiber bridging developed, while its mean value is as big as the case of the $[0_8]_s$. This result further proves that the change in the toughening effect, which is ascribed to the change in the variability in the material properties over the interface, is related to the curing history of the samples of different thicknesses. As a note, we implemented a digital image correlation test on the separately-cured $[0_6 \parallel 0_2]_s$ BB-DCB samples and have shown that there was no displacement gap in the secondary bonding area, further excluding any role of back-bonding in these observations.

2.4. Prolong curing time

This subsection discusses the influence of prolonging the curing time on the toughening mechanism of the sample $[0_8]_s$. Fig. 6(a) and (b) show the force–displacement curve and R-curve of the 2-h cured and 4-h cured $[0_8]_s$, respectively. The reaction force of the 2-h cured $[0_8]_s$ samples was higher than the 4-h cured $[0_8]_s$ samples. The propagation toughness G_{IC}^{prop} of the 2-h cured samples was in the range of 0.7–0.8 N/mm, while that of the 4-h cured $[0_8]_s$ samples was in the range of 0.4–0.45 N/mm. The mean value and standard deviation of the propagation toughness of the 4-h cured $[0_8]_s$ are shown in Table 3. Due to the lack of fiber bridging, its scattering and mean value are both small compared to the cases with extensive fiber bridging. Fig. 6(c) and (d) more intuitively show the fiber bridging extent in the 2-h cured and 4-h cured $[0_8]_s$ samples. Extensive fiber bridging was observed in the incremental crack tip from 120 mm to 140 mm of the 2-h cured $[0_8]_s$ samples. However, for the 4-h cured $[0_8]_s$ samples, there were only a few fibers pulled out at the same range of the incremental crack tip from 120 mm to 140 mm.

2.5. Fiber distribution and fracture surface analysis

In this subsection, we presented the cross-section of two kinds of samples with thicknesses of 1 mm ($[0_2]_s$, which is the core for the separately-cured $[0_6 \parallel 0_2]_s$) and 4 mm ($[0_8]_s$), as shown in Fig. 7. Both of them were cured normally for 2 h at 180 °C. The middle region over the thickness of the $[0_8]_s$ plate was exhibited in Fig. 7(c). The microstructure of these two kinds of samples was compared since they have the biggest difference in Mode I toughness and fiber bridging phenomena, which is observed in Figs. 3 and 4. The microscope image shows the

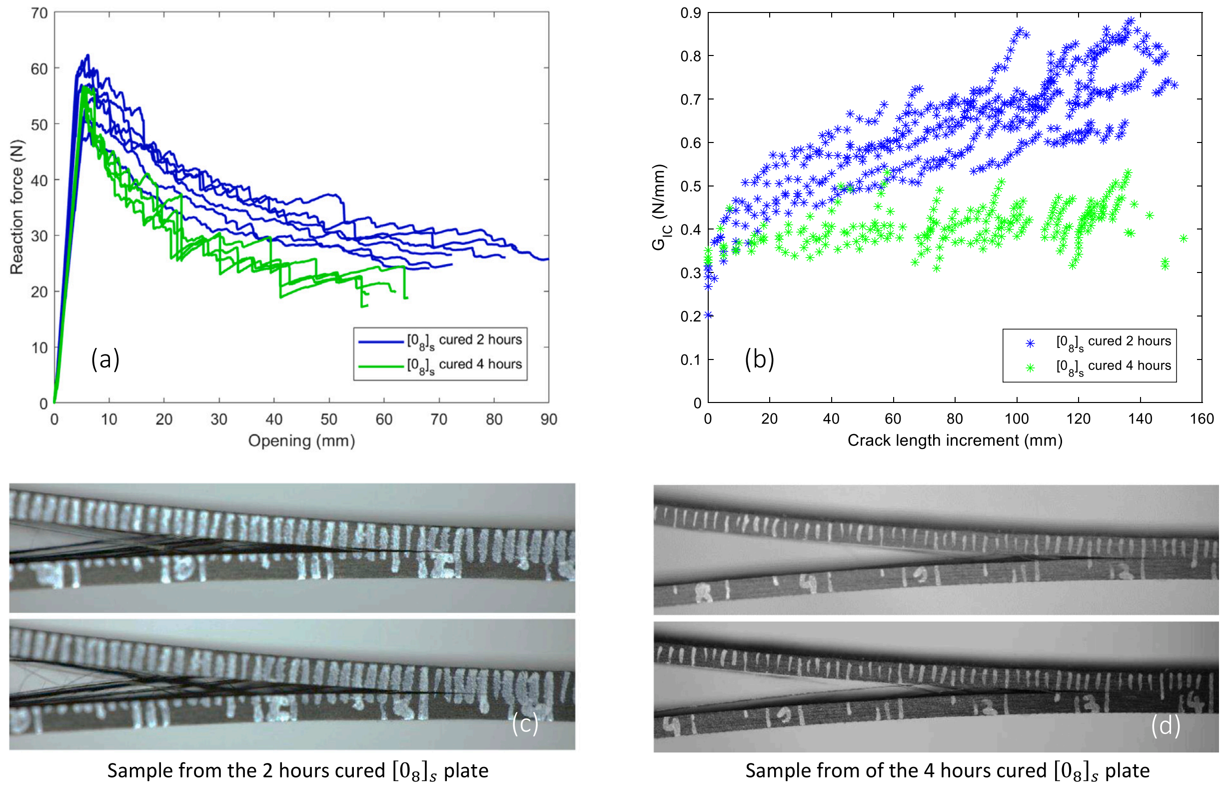

Fig. 6. P-δ curve, R-curve and side view of the 2-h cured and 4-h cured $[0_8]_s$ samples.

constitutions of the T700/M21 material system, which includes carbon fibers with diameter ~7 μm, M21 resin, and thermoplastic particles filled in the resin. A similar microstructure of the T700/M21 composites system was also observed by Sassi et al. [34]. The resin-rich zone in the interlaminar region for the $[0_2]_s$ and $[0_8]_s$ plates was similar to the observed microscope images in Fig. 7. Thus, it is insufficient to attribute the reason for different fiber bridging phenomena to the microstructure of different thicknesses plates with the same curing condition. Although the microscope images check cannot fully guarantee that fiber migration to the neighboring plies did not take place and was one of the reasons for different fiber bridging responses, the possible difference in microstructure could be regarded as one additional source that leads to a variance in the middle interface and thus is considered globally in this study.

Meanwhile, the delamination fracture surfaces were checked with the optical microscope. Fig. 8(a) and (b) are the fracture surfaces from the separately-cured $[0_6 \parallel 0_2]_s$ sample and Fig. 8(c) and (d) are the fracture surfaces from the 2 h cured $[0_8]_s$ sample. Both samples exhibited naked fibers, which indicate the fiber/matrix debonding failure during the DCB delamination process. However, more naked fibers were observed in the fracture surface of the 2 h cured $[0_8]_s$ compared to the separately-cured $[0_6 \parallel 0_2]_s$ sample. The fracture surface of the separately-cured $[0_6 \parallel 0_2]_s$ samples exhibited an intermittent fiber/matrix debond, as shown in Fig. 8(b). While the fracture surface for the 2 h cured $[0_8]_s$ exhibited a continuous fiber/matrix debond. This could further prove the fiber bridging phenomena shown in Fig. 3(a) and (d). A large amount of fiber bridging developed when fibers were pulled out continuously. The intermittent fiber/matrix debond in Fig. 8 could give a reasonable speculation that there is a better fiber/matrix interface, which indicate a more uniform interlaminar property distribution in the separately-cured $[0_6 \parallel 0_2]_s$ samples. This would lead to very few fibers pulled out and more matrix failure during the delamination propagation. The variance in the fiber/matrix interface quality comes from the different curing histories. The following subsection presented the general curing degree of different samples.

2.6. Curing degree results

Fig. 9 shows the heat flux of four different samples. A melting peak was observed corresponding to the thermoplastic particles in the M21 resin around ~200°C. An endothermic behavior took place at the beginning of the curing process. We removed the endothermic peak to calculate the polymerization enthalpy. Therefore, the total enthalpy of the uncured prepreg is calculated as 260 J/g. 2 h 4 mm denotes that the sample is cut from a 4 mm thick plate cured at 180 °C for 2 h. The largest residual enthalpy among the partially cured samples comes from the 2 h 4 mm sample, which is 23.14 J/g with a DoC of 91.1%. The residual enthalpy of the 2 h 1 mm and 4 h 4 mm samples are 8.86 and 14.27 J/g, which gives a DoC of 96.4% and 94.5%, respectively. The results here show a higher DoC for 2 h 1 mm and 4 h 4 mm samples compared to the 2 h 4 mm sample. Note that DSC samples in this work contain carbon fibers T700 and resin M21; thus, the constituent might be slightly different for various sets of samples since the DSC samples are very small, which will cause a change in thermal capacity. Meanwhile, the 2 h 1 mm sample is thinner compared to 2 h 4 mm and 4 h 4 mm samples, which leads to a little bit larger endothermic peak, as shown by the red curve in Fig. 9. Since the DSC samples cover the whole thickness of the CFRP plates, the DSC results were actually the average degree through the thickness. The local degree of cure might obviously features some heterogeneity due to the heterogeneity of the heat flow as well as of the exothermic reaction. However, the sample thickness is relatively thin, which also reduces the possible thickness effect on the residual stress and K_{IC} [35,36]. The local degree of the middle interface of interest for the $[0_8]_s$ sample might be even lower due to the low through-thickness thermal conductivity. Table 4 summarizes the DoC results and sample configurations. The 2 h 1 mm sample is the most representative of the middle fracture surface in contrast to the 2 h 4 mm and 4 h 4 mm samples.

The results show a correlation between the DoC and the fiber bridging extent in mode I fracture behavior. Over cured plates, with a DoC ~96%, have very few fiber bridging triggered during the DCB test,

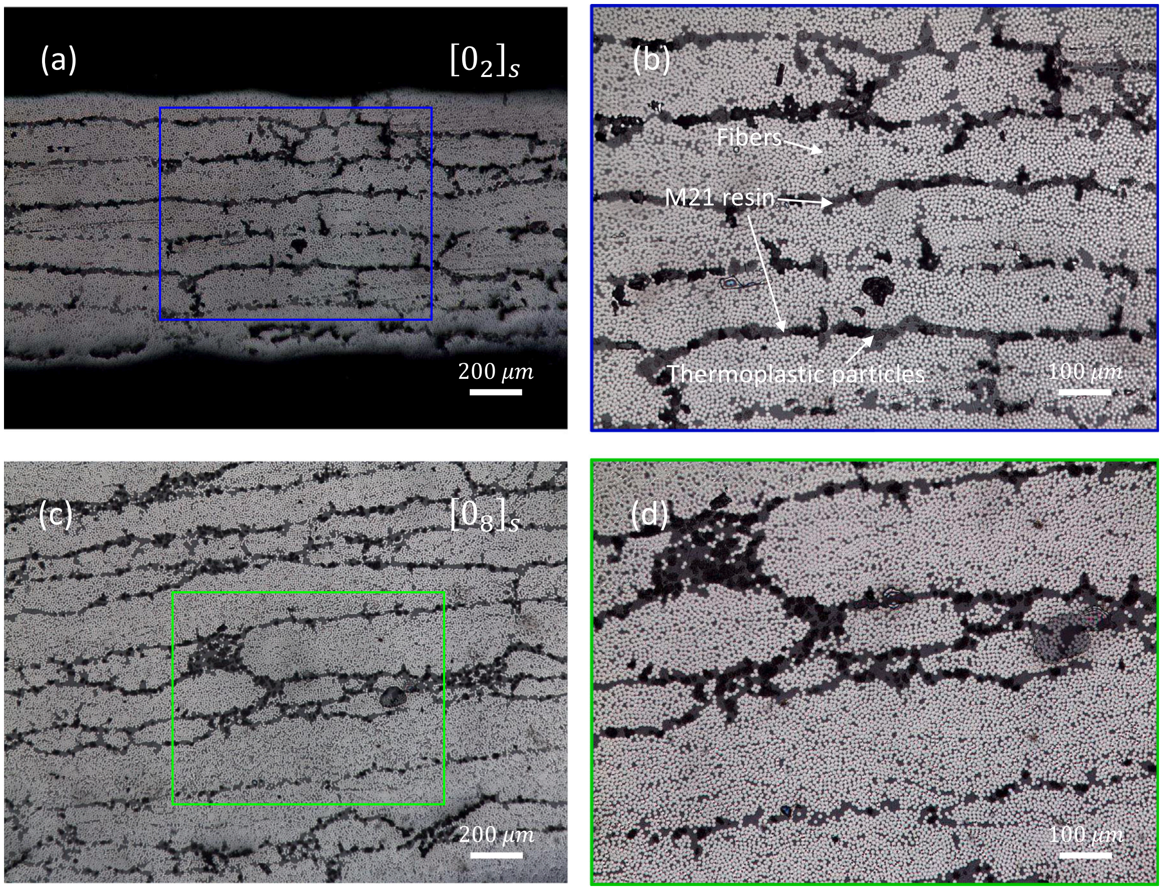

Fig. 7. Cross section of different thickness plates under same curing condition with 2 h hold at 180°C.

Table 4
DoC results and samples configurations.

Sample name	Thickness (mm)	Mass (mg)	DoC
2 h 4 mm	4	6.6	91.1%
2 h 1 mm	1	5.7	94.5%
4 h 4 mm	4	5.8	96.4%

which exhibits a lower stable toughness. The work by Chris et al. [25] shows that samples cured with a dwell stage have a 22% reduction of mode I fracture toughness compared to samples cured with a single-stage cure cycle. A plausible explanation is that over curing a CFRP plat alleviates the heterogeneity of the fiber/matrix interface toughness, which has been proved as an important factor for triggering ligament in secondary bonding [16,18]. The following section studies the influence of the variability of fiber/matrix interface toughness on the extent of fiber bridging through a simple model.

We note that the DoC is the general result of the exothermic reaction in the curing process. While the different bridging phenomena could be attributed to a wide range of reasons, including nesting, lay-up, microstructure, temperature profile over the sample thickness, and curing kinetics [1,5]. These possible reasons could be considered as comprehensive resources of variability in the interlaminar region of DCB samples. The difference of the fracture surface that we observed in Fig. 8 indicates that the interlaminar variance should be large enough to trigger fibers pulled following with a large scale of fiber bridging.

3. Material variability effect on bridging: A qualitative numerical analysis

The previous section illustrated how sensitive is the extent of fiber bridging and the associated toughening effect with respect to the interface curing degree. Aligned with our other works that analyzed the effects of material variability [17,18], our hypothesis is that a lower degree of curing also corresponds to more variables of the interfacial properties, which explains the different bridging responses.

In this section, we adopted an embedded cell approach to further explain the influence of the fiber/matrix interface toughness distribution on the R-curve response. In this work, we assumed that the overall changes made by different curing conditions, *i.e.,* change the plate thickness during curing or prolonging the curing time, could lead to a different level of interlaminar variance. The interlaminar variance, including nesting, fiber migration, microstructure, and curing kinetics, were globally represented in the form of distribution of fiber/matrix interface toughness and strength. This also corresponds to the fracture surface inspection in Fig. 8 that the delamination in DCB tests propagated mainly through the fiber/matrix debond failure.

3.1. Computational model

We utilized an embedded cell approach to study the large-scale bridging explicitly [29,37]. The embedded model includes two elastic DCB arms, fibers represented by beam elements, and connector elements that link the DCB arms and fibers. Thus, instead of using cohesive elements, decohesion behavior was represented by the connector failure. Using strong and weak connectors, where the connector properties follow a Weibull distribution, the fibers could be pulled out, forming a fiber bridging zone. We adopted this approach to study the influence of fiber/matrix interface strength and toughness distribution on the R-curve response.

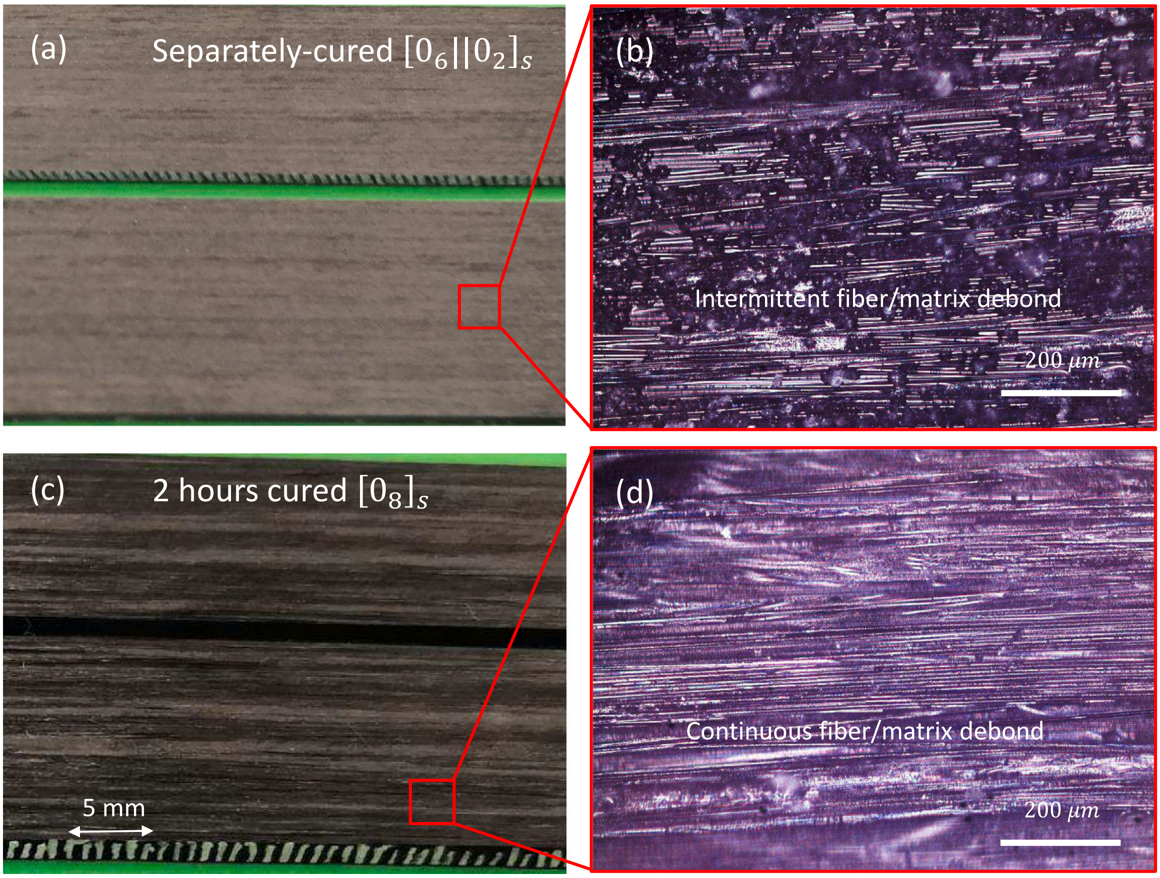

Fig. 8. Fracture surfaces images, (a) and (b): separately-cured $[0_6 \parallel 0_2]_s$, (c) and (d): 2 h cured $[0_8]$ sample.

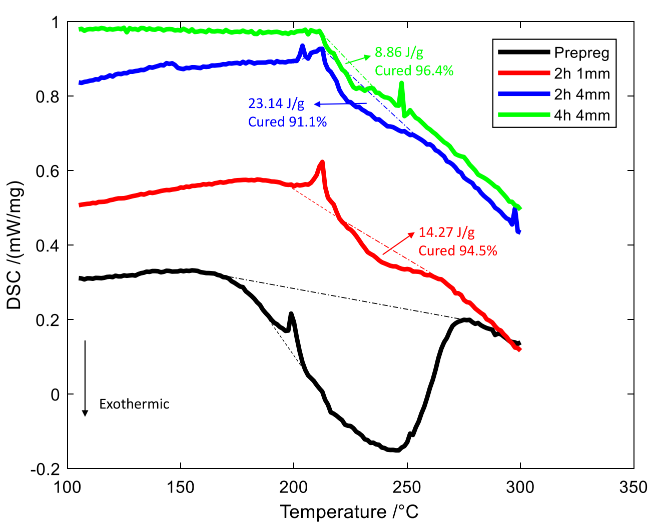

Fig. 9. DSC results and curing degree of the different samples.

Model description

As shown in Fig. 10(a), the embedded model includes three parts: (i) the DCB arms modeled with 3D linear elastic solid elements (C3D8R), (ii) the fibers modeled with 2-noded Timoshenko beam elements (B31), and (iii) connector elements (CONN3D2) that linked the DCB arms and fibers. The mechanical properties of the DCB arms were: E_{11} = 135 GPa, $E_{22} = E_{33}$ = 9.7 GPa, $\nu_{12} = \nu_{13}$ = 0.32, ν_{23} = 0.487, $G_{12} = G_{13}$ = 5.3 GPa, and G_{23} = 3.3 GPa. Only half of the specimen was modeled due to the symmetry. Thus, the CAE model was 10-mm wide.

As shown in Fig. 10(b) and (c), two kinds of linkages were included in this embedded model, either directly between the DCB arms (Fig. 10(c)) or in between each DCB arm and the fibers (representing the bridging fibers) (Fig. 10(b)). To connect the solid mesh of the DCB arms with the nodes of the connector elements, auxiliary fibers with negligible mechanical properties were embedded inside the DCB arms. The connector elements followed a bi-linear traction-separation law. To trigger fiber bridging, the toughness of the connectors linking the real and auxiliary fibers in Fig. 10(b) followed a Weibull distribution with the scale parameter as the initial toughness obtained in the experiments and the different shape parameter k (Eq. (1)). Meanwhile, to mimic the experimental observation, we did not put real fibers over the whole width of the CAE model. As seen in Fig. 10(c), the connectors linking directly the two DCB arms had a uniform toughness. These two linkage kinds were evenly spread over the whole width of the CAE model, as seen in Fig. 10(d). The profile of the beam elements of the fibers was assumed as a circle. The diameter for real fiber and its associated auxiliary fibers was 0.2 mm, while the diameter of the auxiliary fibers that were directly linked to each other was 0.3 mm. Thus, 20 pairs of these two kinds of linkages covered the whole width of the CAE model. In short, the delamination crack propagation will break the uniform connectors and one side of the Weibull distributed connectors, then the beam elements could be pulled out.

The bi-linear traction-separation law of these two kinds of connectors is shown in Fig. 10(e). The initial stiffness was assumed to be 10^8 GPa/m, which is large enough to avoid spurious discontinuity before damage initiation. The initial toughness G_{ini} was set as 0.36 N/mm, which is the experimental toughness, where very limited fiber bridging was observed (Fig. 5). The strength was assumed to be 40

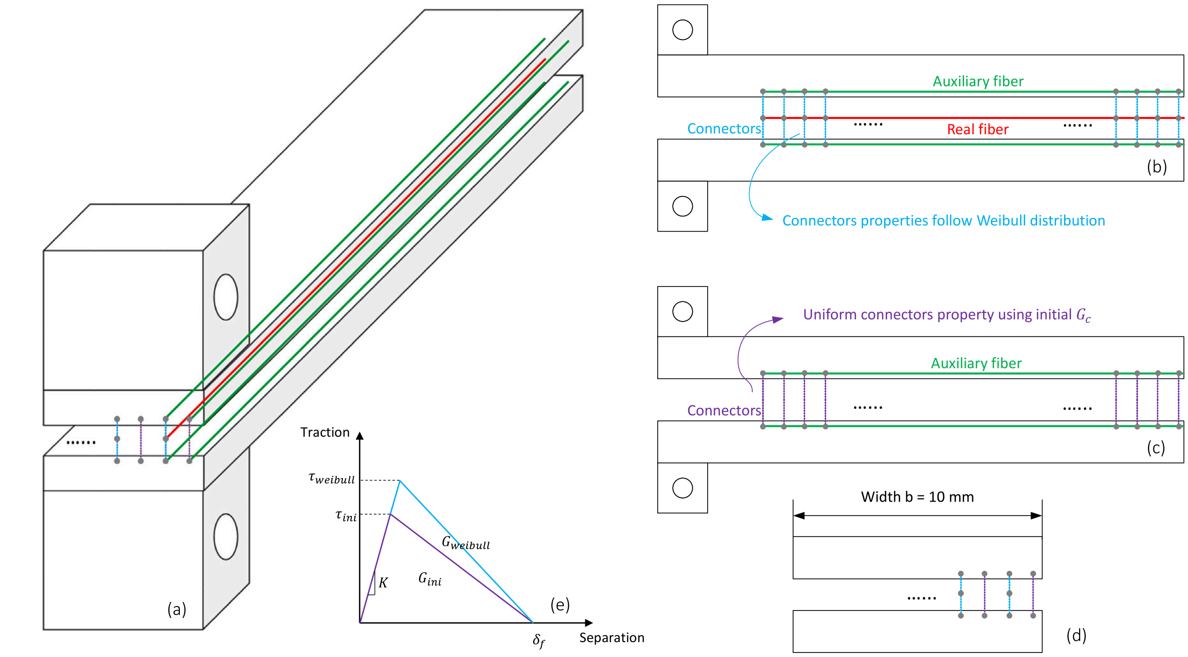

Fig. 10. Schematic of the embedded cell approach.

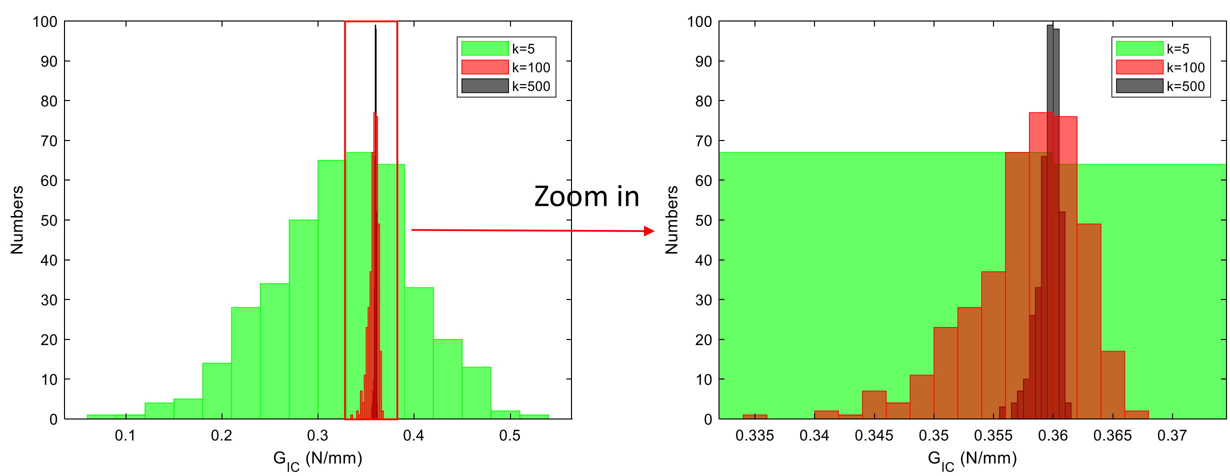

Fig. 11. Variance of the interface property following the Weibull distribution. A larger k means a smaller variance.

MPa. Eq. (1) shows the probability density function of the $G_{weibull}$. The strength $\tau_{weibull}$ followed the same distribution as the toughness $G_{weibull}$. A MATLAB function (wblrnd) was adopted here to generate a list of toughness and strength values that follow this Weibull distribution. Then, the toughness and strength values were assigned to each blue connector. This was to mimic the possible distribution of the interface property in the CFRP plate. By changing the shape parameter k, the influence of the interface variability on the general toughness could be studied.

$$f(G_{weibull}; G_{ini}, k) = \begin{cases} \frac{k}{G_{ini}} \left(\frac{G_{weibull}}{G_{ini}} \right)^{k-1} e^{-(G_{weibull}/G_{ini})^k} & G_{weibull} \geqslant 0 \\ 0 & G_{weibull} < 0 \end{cases} \quad (1)$$

The length of the beam element is set as 0.5 mm to ensure the proper usage of the Timoshenko beam theory. The beam elements of the real fibers were modeled with the same mechanical properties as the DCB arms. To simulate the possible fiber breakage, the failure behavior of the real fibers followed a continuum damage mechanical model with a stress–strain degradation law controlled by the maximum strain, which was implemented through a user-defined subroutine (USDFLD). The maximum stress of the fiber failure initiation was set as 2000 MPa, and the complete failure strain was set as 8.5%, which are the same values used in the work of Canal's et al. [29].

Fig. 11 shows the distribution of the connectors' toughness values following the Weibull distribution under the same scale $G_{ini} = 0.36$ N/mm and with three different shape parameters $k = 5, 100$, and 500. The interface property was quite uniform when $k = 500$. Most of the connectors' toughness values were around the initial toughness value of 0.36. This case corresponds to the uniform distribution of the fiber/matrix interface toughness. $k = 5$ corresponds to a situation in which a large variability of interface properties exists inside the delaminating interface. Several connectors' toughness values were quite as low as ~0.1 N/mm, representing the large defects in the interface during manufacturing. We also chose a medium shape $k = 100$ where the connectors' toughness values were in the range of 0.34–0.365 N/mm.

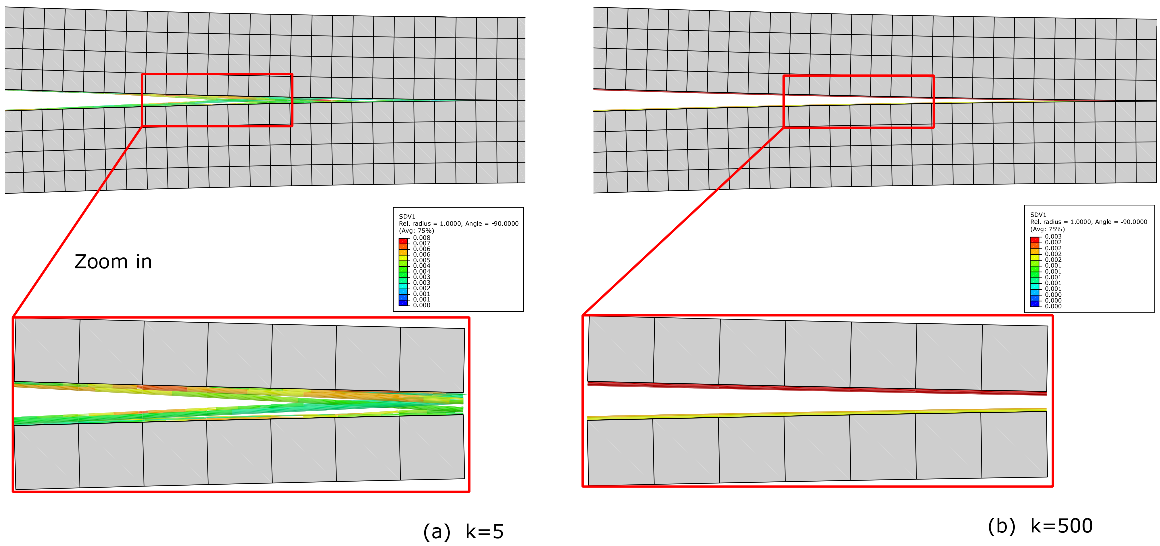

Fig. 12. Simulation results of different interface property distributions taken at the opening of 9.75 mm. The smaller k indicates a larger fiber/matrix interface toughness variance.

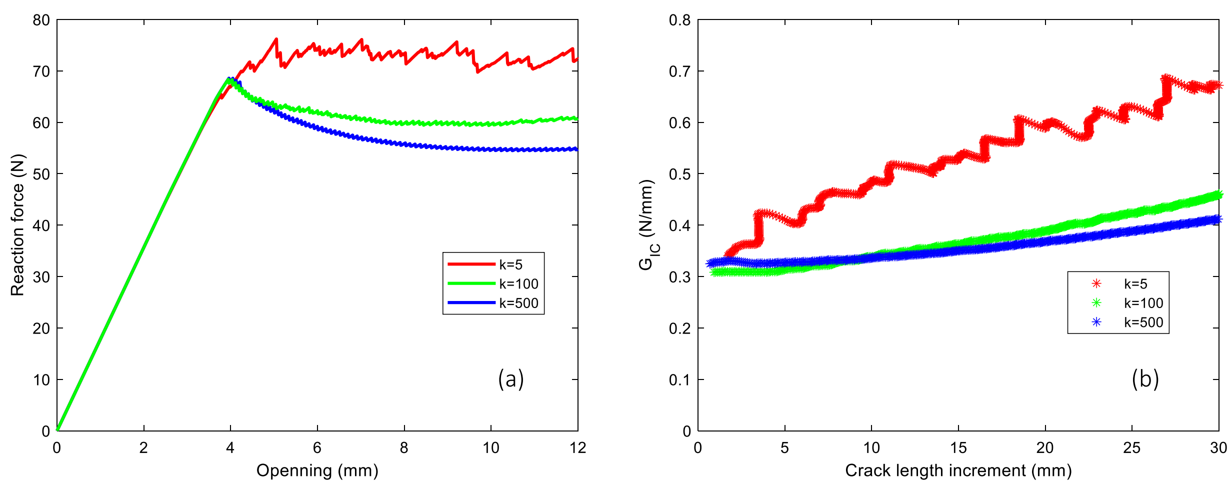

Fig. 13. Reaction force-opening curve and R-curve for different interface property distributions.

3.2. Numerical results and analysis

Fig. 12 shows the bridging phenomena of the two cases ($k = 5$ and $k = 500$) at an opening displacement of 9.75 mm. SDV1 is the damage state of the fibers. There was extensive fiber bridging triggered when $k = 5$, while no fibers were pulled out in the case of $k = 500$. The extra elastic energy stored in the pulled out fibers finally increased the effective propagation toughness in the stable stage of the delamination process.

Fig. 13(a) shows the reaction force with respect to the opening displacement for the three cases with k varying from 5 to 500. Fig. 13(b) shows the calculated R-curve from the $P-\delta$ curve and the delamination crack length. The toughness was quite low ~0.36 N/mm for $k = 500$, where no fiber bridging was triggered, which is the average value of the Weibull distribution for the connectors. For $k = 5$, there was a large variance in the fiber/matrix interface toughness. Thus, significant fiber bridging was triggered, causing an increase in the toughness to a stable plateau of ~0.6 N/mm. The case of $k = 100$ caused a medium result with a propagation G_{IC}^{prop} of ~0.4 N/mm.

4. Conclusions

In this study, a back-bonded DCB test was designed to study the curing process's effect on the development of fiber bridging for plates with various thicknesses. The results showed that thicker core plates cause more fiber bridging in the stable propagation stage. By comparing the results of the co-cured $[0_6 \parallel 0_2]_s$ samples and separately-cured $[0_6 \parallel 0_2]_s$ samples, we have successfully isolated the curing process effect. We found that the different thicknesses of the core plates experienced different curing processes, leading to different bridging developments and fracture toughness values.

Also, prolonging the curing time at 180°C for the $[0_8]_s$ samples alleviated the fiber bridging extent. The fracture surface inspection indicates a better fiber/matrix interface for the separately-cured $[0_6 \parallel 0_2]_s$ compared to the 2 h cured $[0_8]_s$ sample, which is influenced by the curing process. The DSC results showed a correlation between the DoC and the fiber bridging development. A plausible explanation is that over curing CFRP plates causes less heterogeneity in the strength and toughness of fiber/matrix interface, which is one of the main sources for fiber bridging.

An embedded cell approach was also adopted to study the influence of the variance in the fiber/matrix interface toughness on the development of fiber bridging. The larger variance of fiber/matrix toughness exhibited more fiber bridging, leading to a higher effective propagation toughness. Further experimental research on the curing process effect on the property distribution of fiber/matrix interface is needed, as this work highlighted the fact that it can modify damage mechanisms and delamination properties to a large extent.

CRediT authorship contribution statement

Ping Hu: Conceptualization, Performed the experiments and analyzed the data. **Gilles Lubineau:** Conceptualization.

Declaration of competing interest

The authors declare that they have no known competing financial interests or personal relationships that could have appeared to influence the work reported in this paper.

Acknowledgment

The research reported in this publication was supported by funding from King Abdullah University of Science and Technology (KAUST), Saudi Arabia Baseline Research Funds, under award number BAS/1/1315-01-01.

References

[1] Khan R. Fiber bridging in composite laminates: A literature review. Compos Struct 2019;229:111418.
[2] Tamuzs V, Tarasovs S, Vilks U. Progressive delamination and fiber bridging modeling in double cantilever beam composite specimens. Eng Fract Mech 2001;68(5):513–25.
[3] de Moura MFSF, Campilho RDSG, Amaro AM, Reis PNB. Interlaminar and intralaminar fracture characterization of composites under mode I loading. Compos Struct 2010;92(1):144–9.
[4] Gong Y, Zhao L, Zhang J, Wang Y, Hu N. Delamination propagation criterion including the effect of fiber bridging for mixed-mode I/II delamination in CFRP multidirectional laminates. Compos Sci Technol 2017;151:302–9.
[5] Naya F, Pappas G, Botsis J. Micromechanical study on the origin of fiber bridging under interlaminar and intralaminar mode I failure. Compos Struct 2019;210:877–91.
[6] Gong Y, Zhang B, Zhao L, Zhang J, Hu N, Zhang C. R-curve behaviour of the mixed-mode I/II delamination in carbon/epoxy laminates with unidirectional and multidirectional interfaces. Compos Struct 2019;223:110949.
[7] Quan D, Deegan B, Binsfeld L, Li X, Atkinson J, Ivanković A, et al. Effect of interlaying UV-irradiated PEEK fibres on the mechanical, impact and fracture response of aerospace-grade carbon fibre/epoxy composites. Composites B 2020;191:107923.
[8] Zhou H, Du X, Liu H, Zhou H, Zhang Y, Mai Y. Delamination toughening of carbon fiber/epoxy laminates by hierarchical carbon nanotube-short carbon fiber interleaves. Compos Sci Technol 2017;140:46–53.
[9] Garcia EJ, Wardle BL, John Hart A. Joining prepreg composite interfaces with aligned carbon nanotubes. Composites A 2008;39(6):1065–70.
[10] Frossard G, Cugnoni J, Gmür T, Botsis J. An efficient method for fiber bridging traction identification based on the R-curve: Formulation and experimental validation. Compos Struct 2017;175:135–44.
[11] de Morais AB, Pereira AB. Application of the effective crack method to mode I and mode II interlaminar fracture of carbon/epoxy unidirectional laminates. Composites A 2007;38(3):785–94.
[12] Svensson D, Alfredsson KS, Biel A, Stigh U. Measurement of cohesive laws for interlaminar failure of CFRP. Compos Sci Technol 2014;100:53–62.
[13] Farmand-Ashtiani E, Cugnoni J, Botsis J. Specimen thickness dependence of large scale fiber bridging in mode I interlaminar fracture of carbon epoxy composite. Int J Solids Struct 2015;55:58–65.
[14] Frossard G, Cugnoni J, Gmür T, Botsis J. Mode I interlaminar fracture of carbon epoxy laminates: Effects of ply thickness. Composites A 2016;91:1–8.
[15] Johnson WS, Mangalgiri PD. Investigation of fiber bridging in double cantilever beam specimens. J Compos Technol Res 1987;9(1):10–3.
[16] Tao R, Li X, Yudhanto A, Alfano M, Lubineau G. On controlling interfacial heterogeneity to trigger bridging in secondary bonded composite joints: An efficient strategy to introduce crack-arrest features. Compos Sci Technol 2020;188:107964.
[17] Li X, Tao R, Alfano M, Lubineau G. How variability in interfacial properties results in tougher bonded composite joints by triggering bridging. Int J Solids Struct 2020;191–192:87–98.
[18] Li X, Tao R, Yudhanto A, Lubineau G. How the spatial correlation in adhesion properties influences the performance of secondary bonding of laminated composites. Int J Solids Struct 2020;196–197:41–52.
[19] Herráez M, Pichler N, Botsis J. Improving delamination resistance through tailored defects. Compos Struct 2020;247:112422.
[20] Liu W, Chen P. Theoretical analysis and experimental investigation of the occurrence of fiber bridging in unidirectional laminates under Mode I loading. Compos Struct 2021;257:113383.
[21] Han S, Chung DDL. Increasing the through-thickness thermal conductivity of carbon fiber polymer–matrix composite by curing pressure increase and filler incorporation. Compos Sci Technol 2011;71(16):1944–52.
[22] Kandare E, Khatibi AA, Yoo S, Wang R, Ma J, Olivier P, et al. Improving the through-thickness thermal and electrical conductivity of carbon fibre/epoxy laminates by exploiting synergy between graphene and silver nano-inclusions. Composites A 2015;69:72–82.
[23] Li N, Li Y, Hang X, Gao J. Analysis and optimization of temperature distribution in carbon fiber reinforced composite materials during microwave curing process. J Mater Process Technol 2014;214(3):544–50.
[24] Stark W, Jaunich M, McHugh J. Cure state detection for pre-cured carbon-fibre epoxy prepreg (CFC) using Temperature-Modulated Differential Scanning Calorimetry (TMDSC). Polym Test 2013;32(7):1261–72.
[25] Hunt C, Kratz J, Partridge IK. Cure path dependency of mode I fracture toughness in thermoplastic particle interleaf toughened prepreg laminates. Composites A 2016;87:109–14.
[26] Chen C, Nesbitt S, Reiner J, Vaziri R, Poursartip A, Fernlund G. Cure path dependency of static and dynamic Mode II interlaminar fracture toughness of interlayer toughened composite laminates. Compos Sci Technol 2020;108444.
[27] Patel A, Kravchenko O, Manas-Zloczower I. Effect of curing rate on the microstructure and macroscopic properties of epoxy fiberglass composites. Polymers 2018;10(2):125.
[28] Hoffman J, Khadka S, Kumosa M. Determination of gel point and completion of curing in a single fiber/polymer composite. Compos Sci Technol 2020;188:107997.
[29] Canal LP, Pappas G, Botsis J. Large scale fiber bridging in mode I intralaminar fracture. An embedded cell approach. Compos Sci Technol 2016;126:52–9.
[30] ASTMD5528. Standard test method for mode I interlaminar fracture toughness of unidirectional fiber-reinforced polymer matrix composites. ASTM Internat; 2007.
[31] Frossard G, Cugnoni J, Gmür T, Botsis J. Ply thickness dependence of the intralaminar fracture in thin-ply carbon-epoxy laminates. Composites A 2018;109:95–104.
[32] Pappas G, Botsis J. Intralaminar fracture of unidirectional carbon/epoxy composite: experimental results and numerical analysis. Int J Solids Struct 2016;85–86:114–24.
[33] Falzon BG, Hawkins SC, Huynh CP, Radjef R, Brown C. An investigation of Mode I and Mode II fracture toughness enhancement using aligned carbon nanotubes forests at the crack interface. Compos Struct 2013;106:65–73.
[34] Sassi S, Marguerès P, Olivier P, Le Begue R. Determination of anisotropic geometrical parameters for the electrical characterization of carbon/epoxy composite during oven curing. Composites A 2016;80:204–16.
[35] Seers B, Tomlinson R, Fairclough P. Residual stress in fiber reinforced thermosetting composites: A review of measurement techniques. Polym Compos 2021;42(4):1631–47.
[36] Kravchenko OG, Kravchenko SG, Sun CT. Thickness dependence of mode I interlaminar fracture toughness in a carbon fiber thermosetting composite. Compos Struct 2017;160:538–46.
[37] Canal LP, Alfano M, Botsis J. A multi-scale based cohesive zone model for the analysis of thickness scaling effect in fiber bridging. Compos Sci Technol 2017;139:90–8.